Biophysical Journal
Article

Biophysical Society

Geometrical nonlinear elasticity of axon under tension: A coarse-grained computational study

Ning Liu,[1] Poorya Chavoshnejad,[2] Shaoheng Li,[1] Mir Jalil Razavi,[2] Tianming Liu,[3] Ramana Pidaparti,[1] and Xianqiao Wang[1,*]

[1]College of Engineering, University of Georgia, Athens, Georgia; [2]Department of Mechanical Engineering, Binghamton University, Binghamton, New York; and [3]Department of Computer Science, University of Georgia, Athens, Georgia

ABSTRACT Axon bundles cross-linked by microtubule (MT) associate proteins and bounded by a shell skeleton are critical for normal function of neurons. Understanding effects of the complexly geometrical parameters on their mechanical properties can help gain a biomechanical perspective on the neurological functions of axons and thus brain disorders caused by the structural failure of axons. Here, the tensile mechanical properties of MT bundles cross-linked by tau proteins are investigated by systematically tuning MT length, axonal cross-section radius, and tau protein spacing in a bead-spring coarse-grained model. Our results indicate that the stress-strain curves of axons can be divided into two regimes, a nonlinear elastic regime dominated by rigid-body like inter-MT sliding, and a linear elastic regime dominated by affine deformation of both tau proteins and MTs. From the energetic analyses, first, the tau proteins dominate the mechanical performance of axons under tension. In the nonlinear regime, tau proteins undergo a rigid-body like rotating motion rather than elongating, whereas in the nonlinear elastic regime, tau proteins undergo a flexible elongating deformation along the MT axis. Second, as the average spacing between adjacent tau proteins along the MT axial direction increases from 25 to 125 nm, the Young's modulus of axon experiences a linear decrease whereas with the average space varying from 125 to 175 nm, and later reaches a plateau value with a stable fluctuation. Third, the increment of the cross-section radius of the MT bundle leads to a decrease in Young's modulus of axon, which is possibly attributed to the decrease in MT numbers per cross section. Overall, our research findings offer a new perspective into understanding the effects of geometrical parameters on the mechanics of MT bundles as well as serving as a theoretical basis for the development of artificial MT complexes potentially toward medical applications.

SIGNIFICANCE Physical forces acting on axon fibers play an important role in brain neurological functions, especially in brain disorders caused by the structural failure of axons. The question is, how the geometrical parameters of axon, such as average MT length, cross-sectional radius, and tau protein spacing, influence its mechanical performance of axons, remain to be solved. Its answer will help gain an enhanced mechanistic perspective on how natural selection resulted in biological axon geometrical parameters and serve as a theoretical basis for developing artificial MT complexes which can be used for future medical applications.

INTRODUCTION

Recent studies have shown that physical forces are constantly acting on the axon and play an important role in axon physiology (1–3). For instance, moderate axonal forces during development activate axonal elongation and growth (4–6), whereas extreme axonal forces during impact may lead to direct axonal damage and diffuse axonal injury (7,8). In humans, the axon can be up to a meter in length, and consists of a shell skeleton and a microtubule (MT) bundle cross-linked by MT-associated protein (MAP) tau, referred to as "tau proteins" for the remainder of this work (9). Axonal destruction is a characteristic feature of focal and diffuse traumatic brain injury, and can be characterized by local disorientation of the axonal MT bundle, axonal beading, impaired axonal transport, retraction of the synapse, and axonal degeneration (7,10–12). Traumatic axonal injury has been studied through a number of in vitro studies in which axons are subjected to traumatic stretch injury. A recent study shows evidence of MT rupture in the vicinity of axonal beads formed because of a traumatic stretch injury (13). MTs have been shown to rupture at

Submitted January 25, 2021, and accepted for publication July 20, 2021.

*Correspondence: xqwang@uga.edu

Editor: Frauke Graeter.

https://doi.org/10.1016/j.bpj.2021.07.019

strains of ~50% (14). It is possible that the cross-links between MTs, formed by tau proteins, fail under traumatic loading, leading to the characteristic loss of the bundled architecture. The lateral reinforcement of MTs by cross-linking to the cytoskeleton has been shown to enhance their ability to bear compressive loads (15). Though MTs are conventionally regarded as sustaining compressive loads, in certain circumstances, such as in traumatic stretch injury, they are placed in tension. Experimental techniques have yet to characterize the immediate mechanical behavior of axonal MT bundles in tension. Computational modeling techniques have been employed to investigate the mechanical behavior of the filaments comprising the cytoskeleton (16,17) and have been used to investigate cross-linked networks (18–20). These studies have emphasized the importance of the cross-link properties and network/bundle geometry in the overall mechanical behavior. Nonaffine behavior of cytoskeletal networks has been characterized previously, whereby realignment of network fibers leads to overall network stiffening at high stress (21,22). A few studies have investigated the bending mechanics of cross-linked MT bundles. Tolomeo et al. (23) used theoretical and computational modeling to show that the shear resistance provided by cross-links greatly increases MT bundle bending stiffness. Furthermore, a theoretical investigation by Bathe et al. (24) has characterized distinct bundle bending stiffness regimes resulting from the competition between filament stretching and cross-link shearing.

Despite the advances in understanding these underlying mechanisms of the biophysical behavior of axons, it is still an open question as to how these geometrical parameters influence the mechanical performance of axons, which would help to gain a biomechanical perspective on the neurological functions of axons and thus brain disorders caused by the structural failure of axons, such as traumatic brain injury (25) and Alzheimer's disease (26). The first geometrical parameter we consider is the average MT length, or in other words, the MT overlap distance within the axon (L_{OL}) (27,28). For biological composites and their artificial counterparts, overlap distance is among the most important parameters controlling overall mechanical performance, measured by metrics such as Young's modulus, fracture strain, ultimate strength, and toughness, and this parameter can be well explained by the shear-lag model or its derivation (29–34). However, unlike other biocomposites, the stresses between adjacent MTs are transferred through covalent-bond-like tau protein interactions, bringing about nonaffine deformation nature under external force (27). In turn, this nonaffine deformation would bring nonlinearity to stress-strain responses (27,35–37). In addition, the tau protein orientation distribution is a novel metric that can indicate the mechanical performance of MT bundles, indicative of both the overall Young's modulus and enabling a visualization of the transition between linearity and nonlinearity (37). Therefore, the mechanical performance of axons cannot be well described by shear-lag model only. The second geometrical parameter we consider is the tau protein spacing (δ), or in other words, the tau protein density (27,37,38). It has been reported that for large tau protein spacing (small tau protein density) both stiffness and viscosity of the axon quickly decrease to zero under tension, and follow a nonlinear regime (36,39). At higher tau protein density, both effective stiffness and viscosity increase linearly with tau protein density, termed as linear regime (36). However, the tau protein density values which display such a linear regime are not consistent across different studies (36,38). The third geometrical parameter we consider is the axon cross-sectional radius (R). In the adult nervous system, the radii of axons belonging to different tracts can vary by up to two orders of magnitude (50 nm to 5 μm), a result of minimizing energy costs and adaptation to different parts of the body (40). However, it is important to consider how the structural integrity of axons with different radii is maintained during their lifetime. Overall, a comprehensive understanding of the interplay between mechanical properties and geometrical parameters of the axon can provide a better mechanistic understanding of brain disorders, and possibly pave a new perspective for understanding various brain pathologies.

This study seeks to characterize the mechanical behavior of axonal MT bundles in tension. The model emphasizes relevance to biological samples by including the hexagonal bundle architecture, discontinuous MTs, and material parameter predictions, which are based on experimental data. It is proposed that axonal MT bundles exhibit nonlinear mechanical behavior in tension because of nonaffine network deformations. The objective of this study is to explore the interplay of axonal mechanics and structure. Toward this objective, we adopt a bead-spring based coarse grain molecular dynamics model that consists of a network of MTs connected by cross-linking proteins. We systematically varied the average MT length, cross-sectional radius, and tau protein spacing, and characterized the overall mechanical responses as emergent properties of the hierarchical structure.

MATERIALS AND METHODS

Discrete bead-spring models have previously been implemented to describe the mechanical properties of filaments and filamentous networks (19,41–43). A bead-spring coarse-grained model of the axonal MT bundle allows for sufficient system size and complexity but requiring relatively modest computational resources. This type of model also allows for the investigation of irregular, physiologically accurate geometries, providing an essential supplement to theoretical and experimental mechanics studies. Previous studies have focused on bundles with continuous filaments spanning the entire bundle length, despite the fact that biological specimens are not composed in this manner, and thus overlooking the impact of discontinuities on the mechanical properties of the axonal MT bundles. Discontinuities in the MTs can easily be incorporated into the current model, and the role of a variety of geometric and mechanical parameters can thus be investigated. As a result of these considerations, a model of axonal

MT bundles can be developed that closely replicates real cross-linked MT bundles with incorporated spatial and temporal details.

Bead-spring models adequately capture the various types of deformation of filamentous fibers by implementing interaction potentials among beads; these are then calibrated to display certain aspects of mechanical performance under different loading conditions. Fig. 1 *a* shows a schematic representation of an MT bundle using a network of beads connected by springs. The current model is calibrated toward the tension of the bundle under an applied moderate force. This force will quickly elongate the MT bundle across the entropic-dominated regime and into a linear mechanical stretching regime, a transition reported previously (44). Therefore, a linear elastic mechanical bond potential, E_b, is implemented between adjacent MT beads, as expressed using the expression:

$$E_b = k_b \frac{(r - r_0)^2}{2}, \tag{1}$$

where k_b is the bond stiffness constant, r is the bond distance, and r_0 is the equilibrium bond length. The bond stiffness constant k_b can be calibrated by the material properties of the filament in the equation:

$$k_b = \frac{EA}{r_0}, \tag{2}$$

where E is the Young's modulus of the MT and A is the cross-sectional area of the filament. The tau protein cross-links were modeled as two-node linear spring elements, a representation common to a number of cross-linked network models (24).

The bending potential is depicted by a harmonic angle potential as a function of the bending angle θ. The bending potential E_a can be expressed in the form:

$$E_a = k_a \frac{(\theta - \theta_0)^2}{2}, \tag{3}$$

where k_a is the angle spring stiffness constant, θ is the angle between subsequent elements, and θ_0 is the equilibrium angle. The angle spring stiffness constant can be calculated based on the material properties of the filament in the equation:

$$k_b = \frac{EI}{r_0}, \tag{4}$$

where EI is the bending moment of the filament and r_0 is the unstretched bond length. The bending moment EI of an MT can be determined by its persistence length in the equation:

$$EI = l_p k_B T, \tag{5}$$

where $l_p$is the persistence length, k_B is the Boltzmann constant, and T is the temperature. Steric repulsion of the beads in the system is necessary to prevent penetration of the beads within the MTs. The potential associated with the steric repulsion in such a coarse-grained model is only meant to prevent penetration and the form is somewhat arbitrary. A Lennard-Jones potential, E_{nb}, is used:

$$E_{nb} = 4\varepsilon_0 \left[\left(\frac{\sigma_0}{r}\right)^{12} - \left(\frac{\sigma_0}{r}\right)^{6} \right], \tag{6}$$

where ε_0 is the energy-scaling parameter, r is the distance between sterically interacting beads, and σ_0 is the steric radius. The steric radius σ_0 is set to the outer MT diameter, 25 nm, and the potential well ε_0 of 1×10^{-18}N $\times$ m is iteratively selected to prevent penetration with minimal long-range effects. As this potential is merely to prevent penetration and should not cause any long-range effects, a cutoff radius of 1.12 σ is used to truncate the steric repulsion interaction for computational efficiency while preventing filament penetration, which is also widely used in molecular dynamics simulations (29,31–33). We note that exponential potential is also very commonly used in the literature. Additional simulations have been performed using exponential potential. Results can be found in Fig. S1, in which results using Lennard-Jones potential is also presented for comparison. The marginal differences

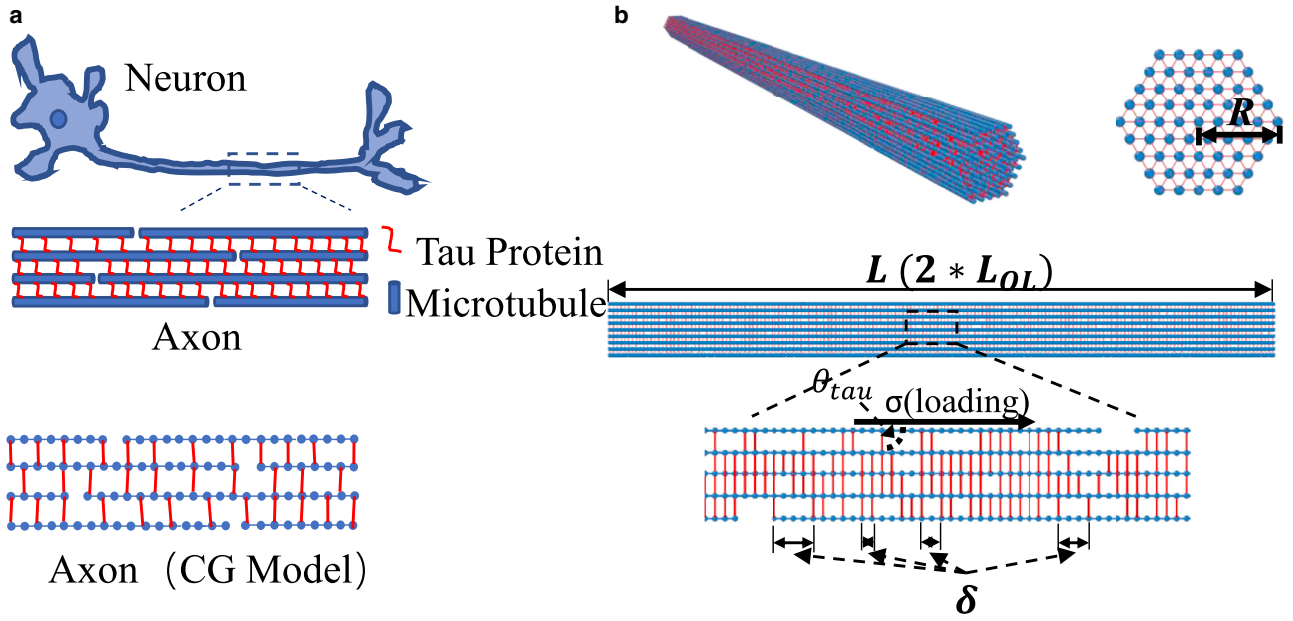

FIGURE 1 (*a*) Schematic view of the structure of axon and its coarse-grained representation. (*b*) Coarse-grained model of an axon and the associated topological parameters (tau protein spacing δ is calculated through averaging the spacing between tau proteins over the whole model using Eq. 7). To see this figure in color, go online.

between stress-strain curves using Lennard-Jones potential and exponential potential justify our choice about the steric repulsion potential.

Using in-house code, a hexagonal bundle of 7–127 MTs with an interlayer spacing of 45 nm (27) is created with the cross-section radius ranging from 45 to 270 nm, which corresponds with an MT area density ranging from 665 to 335 MTs/μm^2. Note that the above density is close to the upper limit reported experimentally, and thus the mechanical performance in this article may be also among the top levels of axon. Each row consists of a set of MTs with a single end-to-end discontinuity along the axial direction. A set of models with various number of MTs, ranging from 14 to 254, are created and the average length of MTs corresponds to half of the length of the model. Also, the end-to-end discontinuities are not placed close to the edges of the bundle by confining them within the length interval from 10 to 90% of the row along the axial direction. The end-to-end discontinuity is set to be 20 nm in length. After the aforementioned model setup, Fig. 1 *b* shows a representative computational model of a MT bundle. The MT bead spacing is set to 10 nm to allow bending between cross-links. Cross-links are pseudorandomly distributed between neighboring MTs throughout the bundle based on the desired average cross-link spacing. The tau cross-link bead mass is added to the mass of the MT bead at the beads where the cross-linking elements were added. The cross-link spacing δ in the bundle is calculated as:

$$\delta = \frac{N_{MT}L}{N_{CL}}, \tag{7}$$

where N_{MT} is the number of MTs, N_{CL} is the number of tau protein cross-links, and L is the average continuous MT length.

In this article, the Langevin equation is used to update the trajectories of particles of axon models,

$$m\frac{d^2\vec{r}}{dt^2} = F_c + F_f + F_r, \tag{8}$$

$$F_f = -\gamma\frac{d\vec{r}}{dt}, \tag{9}$$

$$F_r = \sqrt{\frac{k_BT\gamma}{dt}}\vec{R(t)}, \tag{10}$$

where F_c is the conservative force computed via the usual interactions among beads from MT, F_f is the is a frictional force proportional to the particle's velocity, and F_r is the Brownian forces from solvent at a temperature T. Assume the beads from MT are spherical, the damping coefficient tensor is isotropic and equal to $\gamma = 6\pi\eta r$ according to the Stokes-Einstein equation. In the current model, the dynamic viscosity η is 5.0×10^{-3} Pa.s whereas the radius of the beads r is 10 nm. Therefore, the damping coefficient γ is equal to 9.42×10^{-10} N/(m/s). To accelerate the simulation process and focus on the statics of axon, the damping coefficient in the simulations is shrunk by three orders of magnitude. Relevant simulations are shown here in Fig. S2 to justify our choice about the damping coefficient. In the actual physiological environment, the axon is immersed in the axon cytosol, which could be modeled using anisotropic, hydrodynamics-related friction coefficients. However, because the major focus of this article is on the statics of axon under pure stretch, it should be sufficient to simplify the friction coefficient tensor to be isotropic.

The velocity Verlet algorithm was used to calculate bead trajectories over the duration of each simulation. An axial tensile stress was applied by distributing forces to the ends of the MTs at either end of the bundle. This tensile stress is meant to represent the stress on the MT bundle itself and not necessarily that of the entire axon. These two quantities may not be equal based on the load sharing distribution between all structural components of the axon. The resultant tensile force was first calculated by multiplying the desired tensile stress by the cross-sectional area. This force was then divided evenly among the end beads of the MTs. The total applied force was added in a stepwise fashion to prevent excessive oscillations, whereas the entire model was equilibrated after each force step for 20,000 steps. This stress-controlled loading method can help gain the steady-state responses of axon under external loads, minimizing the loading rate effect on mechanical performance. The open-source software Large-scale Atomic/Molecular Massively Parallel Simulator (LAMMPS) was used to integrate the equations of motion and calculate bead trajectories. A time step of 0.1 ps was used for stability and computational efficiency. The steady-state strain values at a given tensile stress were calculated by allowing the bundle to relax toward a temporarily steady status in a dynamic simulation (i.e., the 10-ns equilibration). Failure strain criteria were enforced for both MTs and tau proteins, based upon which bonds were deleted from the simulation. For MT bonds, the critical strain was set at 0.5 based on experimental measurements of the rupture strain (14). The critical strain of the tau proteins was set to 1.0, corresponding approximately to the jump-out length from a study on tau dimerization by Rosenberg et al. (45) This criterion represents the length at which the tau protein dimers can no longer maintain a bridge between neighboring MTs.

Experimental data from a number of studies were used to assign values to the spring constants in the harmonic potential functions represented in Eqs. 1, 2, 3, 4, 5, and 6. The values of the parameters used in the study are shown in Table 1 and their derivation are detailed in this section. Moreover, Table 2 is also included, which summarizes the scales bridging the physical quantities and associated simulation quantities. Values were chosen to fall within the observed physiological range of axonal MT bundles. Measured values of the elastic modulus of MTs are in the range of several hundred MPa to a few GPa. A thorough study of the anisotropic mechanics of MTs that agreed well with experimental data was performed by Pampaloni et al. (46) A value of 1.5 GPa was used for the MT Young's modulus E_{MT}, which falls within the typical range of reported values and agrees with the Pampaloni study (46). This study also predicted a length-dependent persistence length l_p of MTs. Based on a MT in length 4 μm, a persistence length was predicted to be 420 mm. Using Eq. 5 and this persistence length, an MT flexural rigidity $(EI)_{MT}$ of 1.8×10^{-24} N $\times$ m^2 was obtained.

Another important indication from the Pampaloni study (46) is that MTs are intrinsically curved across different scales. MTs are composed of MT protofilaments, linear polymers of tubulin dimers, in which the curving are controlled by the hydrolysis of GTPs (47). MTs can also form closed loops through kinesin cross-linking proteins, transforming into circular shape structures by equilibrating tension (48). Moreover, under external forces, MTs can be converted into metastable circular states, explaining the recurrent observations of gliding rings in experiments (49). Besides,

TABLE 1 Material parameters of the axon used in the simulations

Parameters	Value
MT Young's modulus, E_{MT}	1.5 GPa[a]
MT persistence length, l_p^{MT}	420 μm[a]
MT flexural rigidity, $(EI)_{MT}$	1.8×10^{-24} N.m^2[a]
Tau protein Young's modulus, E_{tau}	5.0 MPa[b]
MT element length, l_0^{MT}	10 nm[b]
Tau protein element length, l_0^{tau}	45 nm[b]
MT cross-section area, A_{MT}	314 nm^2[b]
Tau protein cross-section area, A_{tau}	1 nm^2[c]
Axon cytosol viscosity, η	5.0×10^{-3} Pa.s[d]
MT axial spring constant, k_s^{MT}	47.1 N/m[e]
MT bending spring constant, k_b^{MT}	1.8×10^{-16} N.m[f]
Tau protein axial spring constant, k_s^{tau}	3.925×10^{-2} N/m[g]

[a]Can be found in (46).
[b]Can be found in (27).
[c]Can be found in (36).
[d]Can be found in (35).
[e]$k_s^{MT} = \frac{E_{MT}A_{MT}}{l_0^{MT}}$.
[f]$k_b^{MT} = \frac{(EI)_{MT}}{l_0^{MT}}$.
[g]$k_s^{Tau} = \frac{E_{Tau}A_{Tau}}{l_0^{Tau}}$.

TABLE 2 Conversion scales between physical values and simulation values

Parameters	Physical value	Simulation value
Timescale, τ[a]	1.0×10^{-11} s	1
Distance scale, σ[a]	1.0×10^{-9} m	1
Mass scale, m[a]	1.0×10^{-22} kg	1
Boltzmann constant, k_B[a]	1.380649×10^{-23} J/K	1
Energy scale, ε[b]	1.0×10^{-18} N.m	1
Stiffness scale, k_0[b]	1.0 N/m	1
Viscosity scale, η_0[b]	1.0×10^{-2} Pa.s	1
Temperature scale, T_0[b]	72,411 K	1
MT axial spring constant, k_s^{MT}	47.1 N/m	47.1
MT bending spring constant, k_b^{MT}	1.8×10^{-16} N.m	180
Tau protein axial spring constant, k_s^{Tau}	3.925×10^{-2} N/m	0.03925
Axon cytosol viscosity, η	5.0×10^{-3} Pa.s	0.5
Physiological temperature, T	310 K	0.0043

[a]The first four scales converting physical values to simulation values are basic scales. Note that, instead of temperature scale, Boltzmann constant is used here as one basic unit, which is widely used in molecular dynamics simulations.
[b]Those scales are derived scales based on the first four basic scales.

the effective binding rate of kinesin proteins affect the formation of MT rings, in which the MT density is also a key factor (50). Both in vivo and in vitro MTs are buckled whereas the buckling modes are different (51). Despite this, MT curving is not discussed in this article because of its marginal influence on the mechanical responses of axon under pure stretch. However, further exploration of MT curving would be necessary for future studies focusing on mechanics of axon beyond pure stretch.

Studies of the mechanical properties of single-dimerized tau protein cross-links are unavailable, so an estimate of the Young's modulus is needed. By estimating a persistence length of tau dimers on the order of a micron and using Eq. 5, a Young's modulus of tau protein cross-links E_{tau} of 5.0 MPa was used. The estimation of this parameter is further complicated because the stretching mode of the cross-link is unclear; the stretching of the tau filaments, the tau-tau bond, or the tau-MT bond are all possible contributors. As such, this value is approximate, but the qualitative bundle behavior should not be significantly altered unless the true modulus is incorrect by multiple orders of magnitude (27).

Using LAMMPS, the stress-strain and failure behavior of axonal MT bundles was investigated. The parameters under investigation, the average cross-link spacing δ, the overlap distance L_{OL}, and the cross-section radius R, were investigated ranging from 25 to 175 nm, 0.5–16 μm, and 45–270 nm, respectively. This range of δ corresponds to values typical of the estimated physiological range. However, no explicit data are available regarding the average cross-link spacing in vivo. As such, the estimated range was based on images of axonal MT bundles cross-linked by MAP tau. This parameter study allowed for the investigation of the effects of increasing the degree of bundling in response to the density of cross-link bridges on a given length of MT. For each instance of a combination of chosen δ, L_{OL}, and R, five MT bundles were generated by randomizing the locations of cross-links and end-to-end discontinuities in each row. These five configurations allowed for statistical significance and prevented skewing the results toward a particular configuration's response. These bundles were then subjected to uniaxial stress parallel with the bundle axis at stress levels ranging from 1 kPa to 7 MPa, and the bundle strain was calculated in each case.

RESULTS AND DISCUSSION

Response of the axon to uniaxial stretching

In this section, a general case of axon stretching is discussed, to describe common mechanical behaviors shared across all models. Before discussions about mechanical responses of axon, the overall axon strain and stress is clearly defined first. The overall axon strain is defined following the similar idea from engineering strain. As shown in Fig. S3 *a*, the initial length and the length after deformation of the axon is l_0 and l, respectively, so the overall axon strain ε can be defined as $\varepsilon = (l - l_0)/l_0$. As shown in Fig. S3 *b*, the force applied on the two ends of axon is F, and the initial cross-section area is A_0. As such, the overall axon stress σ can be defined as $\sigma = F/A_0$.

Here, the tau protein spacing δ is fixed at 25 nm, overlap distance L_{OL} is set to 4 μm, whereas the fiber radius R is fixed at 45 nm. To measure the mechanical properties of the axon, a step wise force-controlled tensile loading method is adopted as described in the previous section; and the results are illustrated in Fig. 2 *a*. In Fig. 2 *b*, the stress-strain response and tau protein orientation of the axon is presented. The stress increases very slowly until the strain approaches 0.5%. As follows, the increase of stress accelerates until the stress shows a constant linear increase with strain. Note that both MTs and tau proteins are linearly elastic; this is reflected in the linear stress-strain relationships evidenced in Fig. 2 *c*. The nonlinear elasticity of the axon originates from its unique topology, wherein the arrangement of the tau proteins, which transfer stress between adjacent MTs, causes nonaffine deformation of the system under external loading. Originally, the tau proteins are relaxed and are aligned perpendicularly to the MTs. Under external loading, the tau proteins then start to rotate as shown in Fig. 2 *b*, with the average orientation of tau proteins θ_{tau} quickly decreasing from 90° to around 60° until the strain reaches to around 0.5%. Adjacent MTs slide along with the rotation of the tau proteins. In this stage, both MTs and tau proteins experience a very small strain. The majority of strain in the axon structure arises from sliding between adjacent MTs. Subsequently, the variance of θ_{tau} is marginal in Fig. 2 *b*, whereas the average strain of tau proteins ε_{tau} increases significantly in Fig. 2 *d*, indicating that the tau proteins are stretched rather than merely being rotated. The averaged strain of tau proteins ε_{tau} have been further divided into axial and lateral components in Fig. S4. Results indicate that axial and lateral components exhibit a linear increase versus overall axon strain as the overall strain is bigger than 1.24%. Despite the nonaffine deformation of tau proteins, the gradual stability of orientation θ_{tau} distribution enables a linear relation between tau protein strain and overall axon strain. Similarly, the MTs themselves also undergo a notable strain in this region. Consequently, the gradual stability of orientation θ_{tau} distribution results in the characteristic linear stress-strain relationship in this stage. Fig. 3 shows the evolution of individual tau protein orientations during the loading process, painting a more distinct picture than the one with the average tau orientation shown in Fig. 2. At the beginning, almost all the tau proteins are perpendicular to the loading direction, measured at 90°.

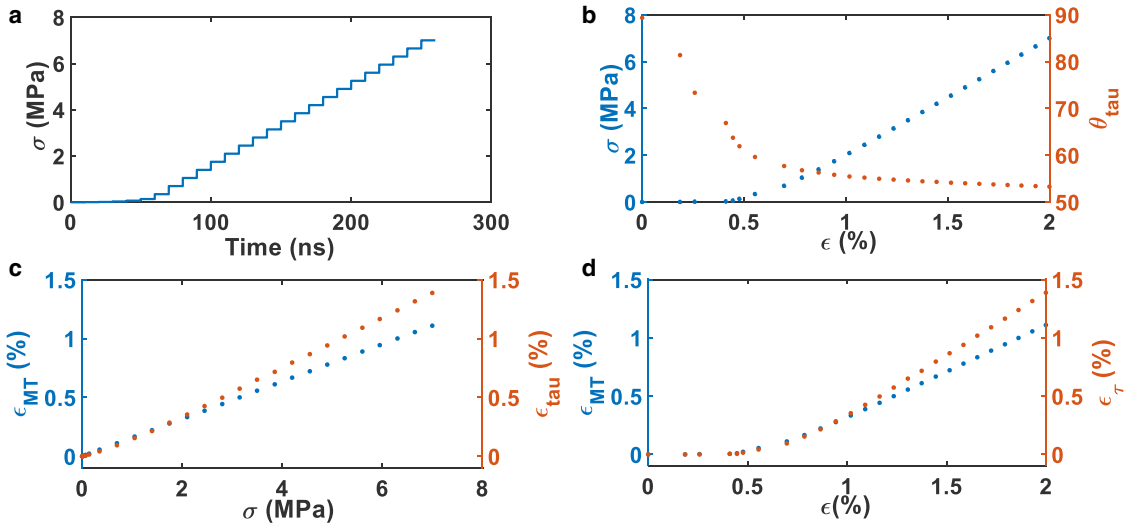

FIGURE 2 (*a*) Axon stress due to the stepwise force-based loading strategy in our uniaxial stretching simulation ($L = 8$ μm, $L_{OL} = 4$ μm, $\delta = 25$ nm, $R =$ 45 nm). (*b*) Axonal stress σ and averaged tau protein orientation θ_{tau} versus axonal strain ε. (*c*) Averaged MT strain (ε_{MT}) and averaged tau protein strain (ε_{tau}) versus σ. (*d*) ε_{MT} and ε_{tau} versus ε. To see this figure in color, go online.

Then, more and more tau proteins rotate under external loading, leading to a widespread spectrum in orientation distribution. After strain ε is greater than 1.24%, the evolving orientation distribution becomes stable with minor changes, coincident with the onset of the linear stress-strain regime of the axon. This finding confirms our conclusion that the gradual stability of orientation θ_{tau} distribution is the origin of transition of the stress-strain relationship in the axon as a whole from nonlinear to linear.

Effect of MT overlap distance

The topology of an axon can be considered as similar to other hierarchical biological materials such as nacre (52), silk (53), and bone (54). In those biological composites, stress transfer is very important for the structural robustness whereas the material overlap distance is one of the most important structural parameters which influence the mechanical properties (55). Although the shear-lag model can be well suited to describe linear elastic properties of many composite materials, the stress transfer mechanism in the axon is different because of the existence of explicit bonds, namely tau proteins (56). Therefore, in this section, the average MT overlap distance L_{OL} is varied to study the effect on tensile mechanical properties of the axon. To further explore the overlap distance effect, uniaxial stretching tests of axon models with different L_{OL}, ranging from 0.5 to 16 μm, have been done, and the corresponding results are shown in Fig. 4. Free strain, defined as strain whereas stress remains below 0.1 MPa, decreases with the increase of L_{OL}. As discussed before, free strain is mainly controlled by nonaffine deformation of geometry, mediated by tau protein rotation. As shown in Fig. 4 *b*, when L_{OL} decreases, the averaged tau protein orientation θ_{tau} reaches a plateau more quickly than the overall strain does, leading to a decreased free strain. Moreover, both the averaged orientation θ_{tau} and averaged strain ε_{tau} of tau proteins experience a narrow strain band with the increase of L_{OL} as shown in Fig. 4, *b and c*. In contrast, the average strain of MT bundles with different L_{OL}-values are close to each other as shown in Fig. S5. This evolution trend results from the variance of the average number of tau proteins per MT. In this section, the average tau protein spacing δ is fixed at 25 nm, so the average number of tau proteins, which are responsible for transferring stress between each pair of adjacent MTs, increases as L_{OL}increases (L_{OL} is half of the overall length of MT L in Eq. 7, whereas the number of MTs N_{MT} is fixed as 7), leading to a decrease in the average load on each tau protein. Therefore, the decrease in force exertion on tau proteins results in a decrease in both the average and variance of θ_{tau} and ε_{tau}. To gain a deeper understanding of overlap distance effect, the shear-lag model is used to describe the relationship between Young's modulus of axon (E_{axon}) and L_{OL} (30,32–34,55). The dependence of E_{axon} on L_{OL} can be expressed as follows:

$$E_{axon} = \frac{E_{max}}{\left(1 + \frac{2l_e^n}{L_{OL}} \coth\left(\frac{L_{OL}}{2l_e^n}\right)\right)}, \tag{11}$$

where E_{max} is the theoretical upper limit for the Young's modulus of an axon with a certain radius (R), L_{OL} is the overlap distance, and $l_e{}^n$is the nominal effective interaction length. In this section, R is set as 45 nm and the cross-section area of axon A_{axon} 5261 nm^2. Therefore, E_{max} can be calculated through the expression below:

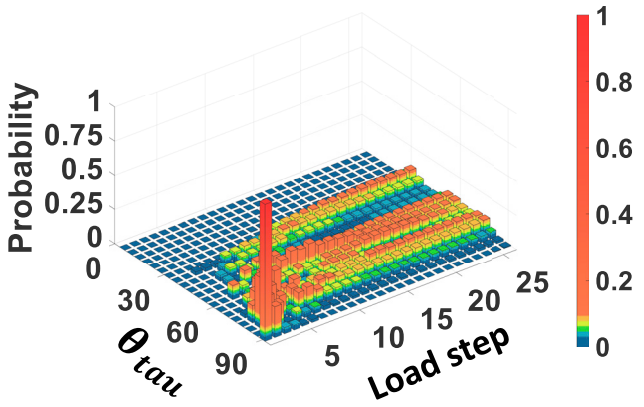

FIGURE 3 Evolution of tau protein orientation distribution under different load steps ($L = 8$ μm, $L_{OL} = 4$ μm, $\delta = 25$ nm, $R = 45$ nm. The small spread of the tau protein orientation for the initial model is smaller than the interval 4.5°). To see this figure in color, go online.

$$E_{max} = \frac{nk_b l_0}{A_{axon}}, \tag{12}$$

where n is the number of MT bond sites, k_b is the stiffness of each MT bond, l_0 is the equilibrium bond length within a MT. Based on Eq. 12, E_{max} is estimated to be 626 MPa.

The shear-lag model has been widely used in biocomposites usually composed of two distinct phases (29–34), namely hard fiber phase and soft matrix phase. The hard fibers are usually placed in a regular staggered manner, whereas the soft matrix are usually filled in the gaps between hard fibers, which is also called "Brick-Mortar" structure. In the original model, the effective interaction length l_e is defined as a characteristic distance in which the axial stress of the hard fiber phase increases dramatically and then saturates at a constant value. To explain the shear-lag model, additional simulations were performed on an idealized axon model with a "Brick-Mortar" structure. Results can be found in Fig. S6 in which relevant discussions are also included. In the idealized shear-lag model, the effective interaction length l_e is uniform given that the hard fibers are identically sized, regularly staggered, and uniformly distributed. However, in the current model, the length of the MTs ranges from 10 to 90% of the overall length of the axon, and thus the observed effective interaction length l_e^{ob} in the axon cannot be uniform accordingly. Then, the nominal effective interaction length l_e^n defined in Eq. 8 can represent the average effect of the observed effective interaction length l_e^{ob}.

The only parameter in Eq. 11 to be determined would be l_e^n, the effective interaction length. From Fig. 4 *d*, it can be estimated to be 0.565 μm through data fitting. Accordingly, if L_{OL} is set to be 4 μm, the average MT length reported in the literature (28), E_{axon} reaches to 80% of E_{max}. Further increasing L_{OL} can only bring limited improvement in the stiffness of axon, which may partially explain the natural selection of L_{OL} to be around 4 μm anatomically. To illustrate the interplay between L_{OL} and E_{axon}, the axial MT strain, ε_{MT}, for two individual MTs is presented for axon models with varying L_{OL} in Fig. 5. There are two gaps for both the central MT (*red curve*) and an edge MT (*blue curve*) because MTs do not extend all the way across the axon (there is a gap for all MTs in the model). More importantly, there is no evident plateau for the strain distribution of both edge and central MTs in Fig. 5, *a and b*. This is in accordance with the interaction length l_e^n being 0.565 μm. Without a sufficiently large L_{OL}, it is impossible for an MT to achieve the theoretical maximal stress status. With L_{OL} increasing, MTs likely experience a prolonged strain plateau as depicted in Fig. 5, *c and d*. Therefore, the strain variance in MTs becomes less significant as L_{OL} increases. Ultimately, the overall Young's modulus of axon can approach the theoretical limit as predicted in Eq. 9 because of nearly homogeneous strain distribution along each individual MT.

Effect of tau protein spacing

In the axon, the most common MAP present is MAP tau, a key component for the load transfer among adjacent MTs. Therefore, the density of tau proteins, being the average spacing between tau proteins δ, should be a critical factor for the structural integrity of the axon. Therefore, this section focuses on studying the effect δ on axonal stiffness and tensile behavior by varying δ from 25 to 175 nm. Note that L_{OL} is fixed at 4 μm, R being 45 nm. For the sake of simplicity and discussion, results for only two extreme cases $\delta = 25$ and $\delta = 175$ nm are presented in Fig. 6, *a–c*. It can be found that with δ increasing, free strain increases, whereas the stiffness decreases. Despite significant changes in the averaged stress-strain curves, the averaged MT strain ε_{MT} is quite similar for $\delta = 25$ and 175 nm. In contrast, both the average tau protein orientation θ_{tau} and average tau protein strain ε_{tau} experience significant changes as δ increases. The differences in geometrical changes for tau proteins and MTs indicate that tau proteins are a major component controlling the mechanical responses of the axon. Moreover, the increasing free strain and decreasing Young's modulus associated with an increase in δ result from the increase of average load-transferring burden for each individual tau protein. In this section, L_{OL} is fixed whereas the averaged spacing of tau proteins δ increases, resulting in decreased number of tau proteins for each pair of adjacent MTs and thus increased force exertion on per tau protein. In Fig. 6 *d*, the Young's modulus E_{axon} decreases as δ increases from 25 to 125 nm. Subsequently, E_{axon} fluctuates around 400 MPa, namely reaching a plateau, as δ increases from 125 to 175 nm. The reason why E_{axon} fluctuates is that the stress per tau protein reaches a plateau, leading to a plateau for strain of tau proteins and thus a plateau in E_{axon}. Overall, Young's modulus E_{axon} decreases as the tau protein spacing δ increases because the increasing load exertion on tau

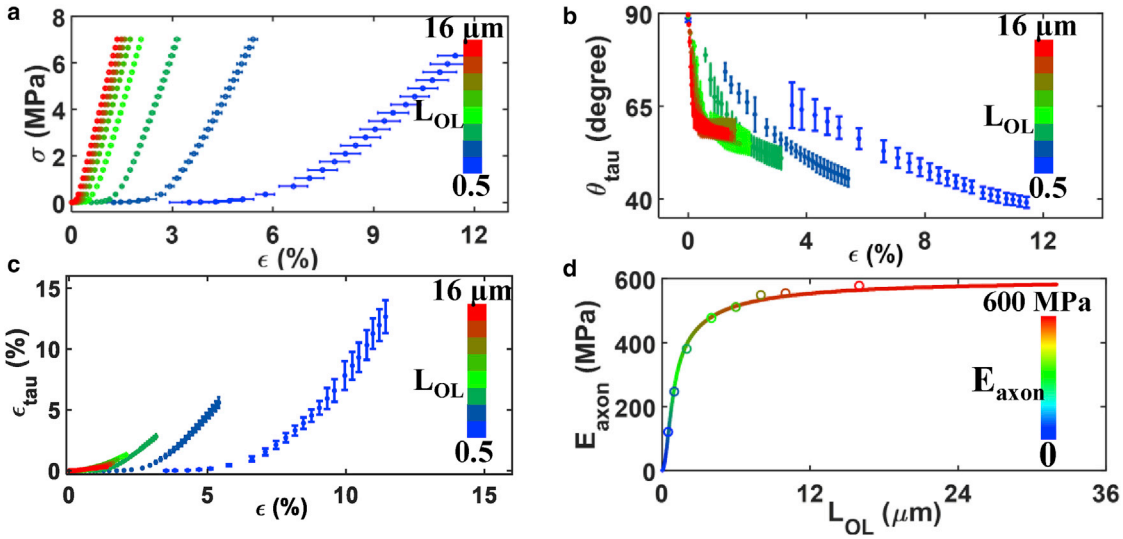

FIGURE 4 (*a*) Stress-strain responses for axon with different L_{OL} (*b*) Tau protein orientation θ_{tau} versus axon strain ε. (*c*) Averaged tau protein strain ε_{tau} versus axon strain ε. (*d*) Young's Modulus E_{axon} versus L_{OL}. To see this figure in color, go online.

proteins leads to greater deformation of tau proteins, thereby softening the model axon.

Effect of axonal fiber diameter

In human axons across different areas of the nervous system, the cross-sectional radius R can differ by up to two orders of magnitude (~0.05–5 μm) (40), resulting from selective pressure to lower biological cost through optimizing information rates. From a mechanistic perspective, it is a critical issue how the axons with different cross-section radii maintain structural integrity. Therefore, this section focuses on investigating the effect of the cross-sectional radius R of the axon model, ranging from 45 to 360 nm, i on the tensile properties of the axon. Note that L_{OL} is fixed at 4 μm, and δ being 25 nm. Fig. 7 *a* shows the stress-strain curves for axon models with different R. It can be seen that there are very clearly two stages of stress response, a nonlinear strain-hardening stage, and a linear stage, the same as the stress-strain curves discussed in the previous sections. In the nonlinear stage, the stress responses are similar to each other even as R increases; this similarity is because of the majority of the stress arising from tau protein rotation independent of R. In contrast, the axonal stress in the linear regime is markedly lower for models with large R, indicating a decreasing trend in the linear-stage Young's modulus. Note that the theoretical limit of E_{axon}, E_{max}, for R = 45 nm, is 626 MPa as mentioned in section 3.1, whereas for R = 270 nm it is 316 MPa. The above difference in theoretical limits of E_{axon} for different R is the consequence of decreasing MT number density per cross section. The decreasing MT number density results from the discrete nature of MT distribution on the cross section. The cross-sectional radius R can be considered as a variable based on the previously used R_0, equal to 45 nm (a central MT and 1 set of surrounding MTs). For $R = nR_0$, the MT number density $\rho_{MT} = \frac{n}{A_{axon}} = \frac{\left(\left(\frac{R}{R_0}\right)\times\left(\left(\frac{R}{R_0}\right)+1\right)\times 3+1\right)}{R^2\times 3\times\sqrt{3}}$. Therefore, ρ_{MT} decreases similar to the form R^{-1}, whereas the theoretical limit for Young's modulus decreases in the same manner. Similarly, E_{max}, the theoretical upper limit for axon with radius R, also follows a similar pattern. As we can see in Fig. 7 *b*, E_{axon} is inversely proportional to R. However, the ratio of E_{axon} over the theoretical limit E_{axon} decreases as R increases, which is caused by density decrease of tau proteins as shown in Figs. S7 and S8. As shown in Fig. S8, MTs can be classified into central and edge MTs, in which the central MTs have been colored blue. The edge MTs with different color have different nearest neighbors. Note that two discontinuous MTs at the same MT site share the same MT index. It can be seen that for model axon with R 45 nm, mean of the tau protein number for central MT is 960 and that for edge MT is 587, in which the ratio is around 1.63. As R increases, number of central MTs, those with six nearest neighbors, also increases while the difference among tau protein number also decreases, 1.40 for axon with R 270 nm. Therefore, the decreasing difference of tau protein number leads to the decrease ofE_{axon} over the theoretical limit E_{max} decreases as R increases. Overall, the decrease of E_{axon} versus increase of R results from both the decreasing density of MTs per cross section and the decreasing difference of tau protein number.

Effect of tau protein orientation

In this section, the initial orientation angle of tau proteins $\theta_{tau}{}^0$ is varied to study its effect on mechanical performance

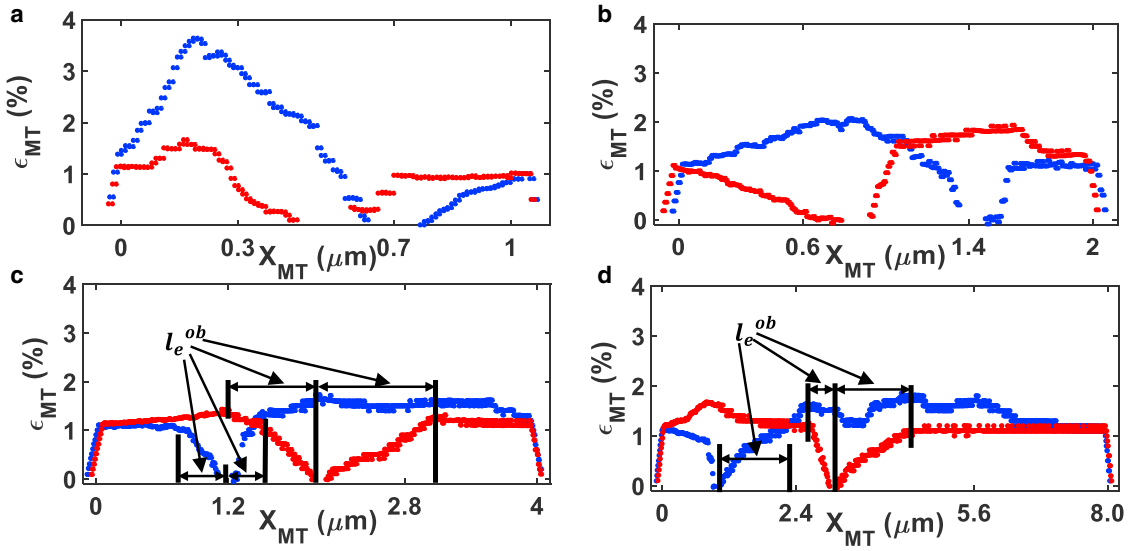

FIGURE 5 Strain distribution along the long axis of two MTs in the axon (the *blue curve* is for the central MT of the axon while the *red curve* is for the edge MT of the axon) for L_{OL} equal to (*a*) 0.5 μm, (*b*) 1 μm, (*c*) 2 μm, and (*d*) 4 μm. R = 45 nm and δ = 25 nm. To see this figure in color, go online.

of axon. As shown in Fig. 8 *a*, red lines represent those tau proteins with initial orientation angles ${\theta_{tau}}^0$ smaller than 90°. As ${\theta_{tau}}^0$ decreases, the tau proteins have an increasing tendency to align along the axial direction of the axon. First, the overlapped distance L_{OL} is fixed at 4 μm. In Fig. 8 *b*, the stress-strain curves of axon with different ${\theta_{tau}}^0$ are shown, showing an evolving pattern in mechanics of axon. As ${\theta_{tau}}^0$ decreases, axons experience a transition from J-shape nonlinear elasticity to linear elasticity. As discussed in the previous section, when ${\theta_{tau}}^0$ is equal to 90°, the tau proteins should first rotate and then elongate under axial tension of axon, ultimately leading to the J-shape nonlinear elasticity. As ${\theta_{tau}}^0$ decreases, the initiation of elongation of tau proteins becomes quicker, leading to a decreasing free-strain stage. Therefore, when the cotangential of ${\theta_{tau}}^0$ is bigger than 40/45, the free-strain stage disappears and thus the axons become linear elastic. Moreover, the stress-strain curves are nearly identical for $\cot({\theta_{tau}}^0) = 60/45$ and 80/45. The Young's modulus of axons E_{axon} with different ${\theta_{tau}}^0$ were obtained and shown in Fig. 8 *b*. Note that E_{axon} of J-shape stress-strain curves are calculated based on the final linear stage. It can be seen that E_{axon} decreases first, then increases, and finally approaches a plateau as ${\theta_{tau}}^0$ decreases. To investigate the effect of overlapped distance L_{OL}, the overlapped distance L_{OL} was varied, whereas ${\theta_{tau}}^0$ was fixed. As the overlapped distance L_{OL} decreases,

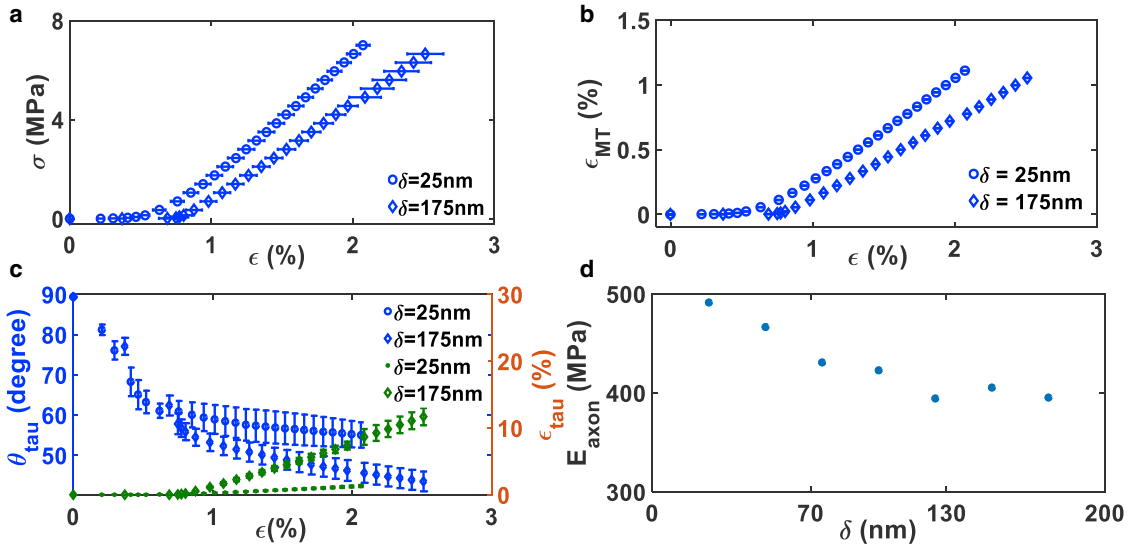

FIGURE 6 (*a*) Stress-strain responses for axon with different tau protein spacing δ. (*b*) Average MT strain ε_{MT} versus axon strain ε. (*c*) Averaged tau protein orientation θ_{tau} and tau protein strain ε_{tau} versus overall strain ε. (*d*) Young's modulus E_{axon} versus tau protein spacing δ. $L = 8$ μm, $L_{OL} = 4$ μm, $R =$ 45 nm. To see this figure in color, go online.

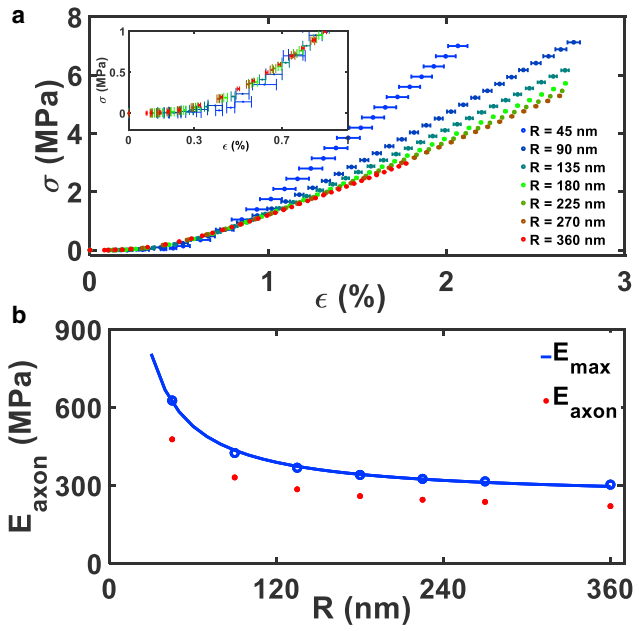

FIGURE 7 (*a*) Stress-strain curves for axon models with different cross-section radius R. (*b*) Young's modulus of the axon versus cross-section radius R, and comparison with the theoretical limit E_{max} for a given R. $L = 8$ μm, $L_{OL} = 4$ μm, $\delta = 25$ nm. To see this figure in color, go online.

the free-strain stage keeps lengthening and the slope of the final linear stage keeps decreasing, indicating softening axons. As discussed in the previous section, when the overlapped distance is not sufficiently long, the stress-distribution inside axon is far from uniform and the stiffness of MTs cannot be fully utilized. Overall, the initial orientation angle of tau proteins $\theta_{tau}{}^0$ is an important factor controlling the mechanical performance of axons.

CONCLUSIONS

In summary, the mechanical properties of the axon, composed of bundles of MT cross-linked by tau proteins, were investigated through coarse grain molecular dynamics simulations. Geometrical parameters such as overlap distance L_{OL}, cross-sectional radius R, and tau protein spacing δ, were systematically varied to explore their effect on the tensile mechanical properties of the axon. First, the mechanical response of the axon under tension can be divided into two stages, a nonlinear strain-hardening stage, and a linear elastic stage. In the nonlinear strain-hardening stage, the stress increases very slowly because of the nonaffine deformation of tau proteins, mostly through rotation and MT sliding. The average orientation of tau proteins decreases from 90° (perpendicular to the loading direction) to somewhere around 50°, whereas both MTs and tau proteins experience a minor strain, indicating that the deformation in this stage is mainly contributed by rigid-body like motion and structural deformation rather than component strain. In the linear elastic stage, the stress on the axon and the individual components increases linearly with strain. Moreover, the average orientation of tau proteins undergoes relatively small change during this stage, whereas the strain of the MTs and tau proteins increases dramatically, indicating that the mechanical behavior of the axon in this stage is dominated by the material stretch of the individual components. As MT

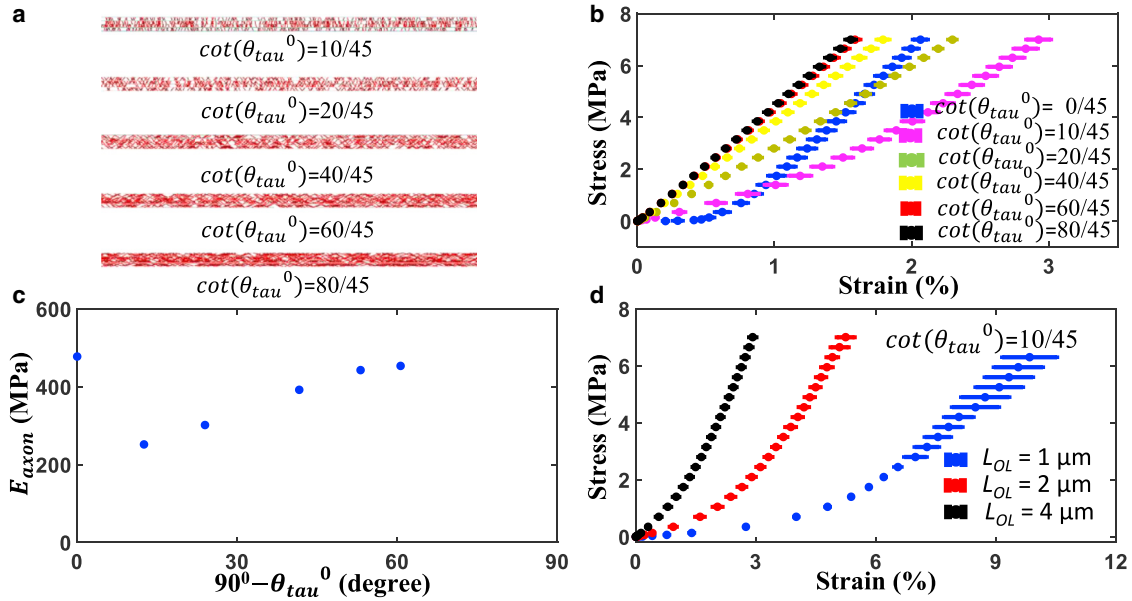

FIGURE 8 Mechanical responses of axon models with different initial orientations of tau proteins θ^0_{tau} under pure stretch (*a*) Overview of axon models (*b*) Stress-strain curves for axon models (*c*) Young's modulus E_{axon} of axon models (*d*) Stress-strain curves of axon models with different overlapped distance L_{OL} and identical θ^0_{tau}. (The axon models are all 4 μm in overlap distance L_{OL} except (*d*), 45 nm in cross-section radius R, and 25 nm in tau protein spacing δ). To see this figure in color, go online.

overlap distance L_{OL} increases, the axonal Young's modulus E_{axon} increases and gradually reaches the theoretical limit, which is also in good agreement with the shear-lag model. In addition, for L_{OL}= 4 μm, the average value as reported in the literature, E_{axon} is ~80% of the theoretical limit, ensuring the structural integrity of axon. This could be a partial explanation for the natural selection and development of this MT length, which corresponds directly to L_{OL}. Secondly, as the tau protein spacing δ is increased from 25 to 125 nm, E_{axon} decreases almost linearly. Subsequently, as the tau protein spacing δ is increased further from 125 to 175 nm, Young's modulus of axon E_{axon} only fluctuates around the plateau value. The decreasing trend of E_{axon} versus the increase of δ results from the increase of the average load per tau protein, and thus leads to an increased deformation of the tau proteins. Thirdly, as the cross-section radius R increases, E_{axon} decreases because of the decreased density of MT number over the cross section. Overall, these research findings provide an enhanced mechanistic perspective on how natural selection resulted in biological axon geometrical parameters. In addition, these findings can serve as a theoretical basis for developing artificial MT complexes that can be used for future medical applications. In the future, the geometrical parameters of axons can be measured in real axons of animal or human brains via biological experiments, and those measurements in different brain regions, such as cortical gyri and sulci, could be potentially used for exploration of related neuroscience questions, e.g., interplay of axonal wiring and neural growth in cortical folding mechanisms.

SUPPORTING MATERIAL

Supporting material can be found online at https://doi.org/10.1016/j.bpj.2021.07.019.

AUTHOR CONTRIBUTIONS

X.W. and R.P. designed and guided the presented idea. N.L. performed simulations and analyzed data. P.C. helped analyze data. S.L. helped run simulations. T.L. and M.J.R. contributed to the interpretation of results. All authors discussed the results and contributed to the final manuscript.

ACKNOWLEDGMENTS

N.L., R.P., and X.W. acknowledge the support from the National Science Foundation, United States (Grant No. CMMI-1610812). T.L. and X.W. acknowledges supports from National Science Foundation, United States (Grant No. 2011369). Computational simulations are performed at the University of Georgia Advanced Computing Resource Center.

REFERENCES

1. Koser, D. E., A. J. Thompson, …, K. Franze. 2016. Mechanosensing is critical for axon growth in the developing brain. *Nat. Neurosci.* 19:1592–1598.
2. Franze, K., P. A. Janmey, and J. Guck. 2013. Mechanics in neuronal development and repair. *Annu. Rev. Biomed. Eng.* 15:227–251.
3. Suter, D. M., and K. E. Miller. 2011. The emerging role of forces in axonal elongation. *Prog. Neurobiol.* 94:91–101.
4. Betz, T., D. Koch, …, J. A. Käs. 2011. Growth cones as soft and weak force generators. *Proc. Natl. Acad. Sci. USA.* 108:13420–13425.
5. Holland, M. A., K. E. Miller, and E. Kuhl. 2015. Emerging brain morphologies from axonal elongation. *Ann. Biomed. Eng.* 43:1640–1653.
6. Lamoureux, P., R. E. Buxbaum, and S. R. Heidemann. 1989. Direct evidence that growth cones pull. *Nature.* 340:159–162.
7. van den Bedem, H., and E. Kuhl. 2015. Tau-ism: the Yin and Yang of microtubule sliding, detachment, and rupture. *Biophys. J.* 109:2215–2217.
8. Spires-Jones, T. L., W. H. Stoothoff, …, B. T. Hyman. 2009. Tau pathophysiology in neurodegeneration: a tangled issue. *Trends Neurosci.* 32:150–159.
9. Pannese, E. 2015. Neurocytology: Fine Structure of Neurons, Nerve Processes, and Neuroglial Cells. Springer, Cham.
10. Park, E., J. D. Bell, and A. J. Baker. 2008. Traumatic brain injury: can the consequences be stopped? *CMAJ.* 178:1163–1170.
11. Lu, W., P. Fox, …, V. I. Gelfand. 2013. Initial neurite outgrowth in Drosophila neurons is driven by kinesin-powered microtubule sliding. *Curr. Biol.* 23:1018–1023.
12. Baas, P. W., and F. J. Ahmad. 2001. Force generation by cytoskeletal motor proteins as a regulator of axonal elongation and retraction. *Trends Cell Biol.* 11:244–249.
13. Tang-Schomer, M. D., A. R. Patel, …, D. H. Smith. 2010. Mechanical breaking of microtubules in axons during dynamic stretch injury underlies delayed elasticity, microtubule disassembly, and axon degeneration. *FASEB J.* 24:1401–1410.
14. Janmey, P. A., U. Euteneuer, …, M. Schliwa. 1991. Viscoelastic properties of vimentin compared with other filamentous biopolymer networks. *J. Cell Biol.* 113:155–160.
15. Brangwynne, C. P., F. C. MacKintosh, …, D. A. Weitz. 2006. Microtubules can bear enhanced compressive loads in living cells because of lateral reinforcement. *J. Cell Biol.* 173:733–741.
16. Chandran, P. L., and M. R. K. Mofrad. 2009. Rods-on-string idealization captures semiflexible filament dynamics. *Phys. Rev. E Stat. Nonlin. Soft Matter Phys.* 79:011906.
17. Mofrad, M. R. K. 2008. Rheology of the cytoskeleton. *Annu. Rev. Fluid Mech.* 41:433–453.
18. Silber, J., J. Cotton, …, W. Grant. 2004. Computational models of hair cell bundle mechanics: III. 3-D utricular bundles. *Hear. Res.* 197:112–130.
19. Kim, T., W. Hwang, and R. D. Kamm. 2009. Computational analysis of a cross-linked actin-like network. *Exp. Mech.* 49:91–104.
20. Claessens, M. M. A. E., M. Bathe, …, A. R. Bausch. 2006. Actin-binding proteins sensitively mediate F-actin bundle stiffness. *Nat. Mater.* 5:748–753.
21. Head, D. A., A. J. Levine, and F. C. MacKintosh. 2003. Deformation of cross-linked semiflexible polymer networks. *Phys. Rev. Lett.* 91:108102.
22. Onck, P. R., T. Koeman, …, E. van der Giessen. 2005. Alternative explanation of stiffening in cross-linked semiflexible networks. *Phys. Rev. Lett.* 95:178102.
23. Tolomeo, J. A., and M. C. Holley. 1997. Mechanics of microtubule bundles in pillar cells from the inner ear. *Biophys. J.* 73:2241–2247.
24. Bathe, M., C. Heussinger, …, E. Frey. 2008. Cytoskeletal bundle mechanics. *Biophys. J.* 94:2955–2964.
25. Ghajar, J. 2000. Traumatic brain injury. *Lancet.* 356:923–929.
26. Kanaan, N. M., G. F. Pigino, …, G. A. Morfini. 2013. Axonal degeneration in Alzheimer's disease: when signaling abnormalities meet the axonal transport system. *Exp. Neurol.* 246:44–53.

27. Peter, S. J., and M. R. K. Mofrad. 2012. Computational modeling of axonal microtubule bundles under tension. *Biophys. J.* 102:749–757.
28. Yu, W., and P. W. Baas. 1994. Changes in microtubule number and length during axon differentiation. *J. Neurosci.* 14:2818–2829.
29. Liu, N., X. Zeng, …, X. Wang. 2016. Tough and strong bioinspired nanocomposites with interfacial cross-links. *Nanoscale.* 8:18531–18540.
30. Wei, X., M. Naraghi, and H. D. Espinosa. 2012. Optimal length scales emerging from shear load transfer in natural materials: application to carbon-based nanocomposite design. *ACS Nano.* 6:2333–2344.
31. Liu, N., R. Pidaparti, and X. Wang. 2017. Mechanical performance of graphene-based artificial nacres under impact loads: a coarse-grained molecular dynamic study. *Polymers (Basel).* 9:134.
32. Liu, N., J. Hong, …, X. Wang. 2017. Fracture mechanisms in multi-layer phosphorene assemblies: from brittle to ductile. *Phys. Chem. Chem. Phys.* 19:13083–13092.
33. Xia, W., L. Ruiz, …, S. Keten. 2016. Critical length scales and strain localization govern the mechanical performance of multi-layer graphene assemblies. *Nanoscale.* 8:6456–6462.
34. Chen, B., P. D. Wu, and H. Gao. 2009. A characteristic length for stress transfer in the nanostructure of biological composites. *Compos. Sci. Technol.* 69:1160–1164.
35. de Rooij, R., and E. Kuhl. 2018. Physical biology of axonal damage. *Front. Cell. Neurosci.* 12:144.
36. de Rooij, R., K. E. Miller, and E. Kuhl. 2017. Modeling molecular mechanisms in the axon. *Comput. Mech.* 59:523–537.
37. de Rooij, R., and E. Kuhl. 2018. Microtubule polymerization and cross-link dynamics explain axonal stiffness and damage. *Biophys. J.* 114:201–212.
38. Lazarus, C., M. Soheilypour, and M. R. K. Mofrad. 2015. Torsional behavior of axonal microtubule bundles. *Biophys. J.* 109:231–239.
39. Jakobs, M., K. Franze, and A. Zemel. 2015. Force generation by molecular-motor-powered microtubule bundles; implications for neuronal polarization and growth. *Front. Cell. Neurosci.* 9:441.
40. Perge, J. A., J. E. Niven, …, P. Sterling. 2012. Why do axons differ in caliber? *J. Neurosci.* 32:626–638.
41. Rodney, D., M. Fivel, and R. Dendievel. 2005. Discrete modeling of the mechanics of entangled materials. *Phys. Rev. Lett.* 95:108004.
42. Bertaud, J., Z. Qin, and M. J. Buehler. 2010. Intermediate filament-deficient cells are mechanically softer at large deformation: a multi-scale simulation study. *Acta Biomater.* 6:2457–2466.
43. Sandersius, S. A., and T. J. Newman. 2008. Modeling cell rheology with the subcellular element model. *Phys. Biol.* 5:015002.
44. Blundell, J. R., and E. M. Terentjev. 2009. Stretching semiflexible filaments and their networks. *Macromolecules.* 42:5388–5394.
45. Rosenberg, K. J., J. L. Ross, …, J. Israelachvili. 2008. Complementary dimerization of microtubule-associated tau protein: implications for microtubule bundling and tau-mediated pathogenesis. *Proc. Natl. Acad. Sci. USA.* 105:7445–7450.
46. Pampaloni, F., G. Lattanzi, …, E.-L. Florin. 2006. Thermal fluctuations of grafted microtubules provide evidence of a length-dependent persistence length. *Proc. Natl. Acad. Sci. USA.* 103:10248–10253.
47. Elie-Caille, C., F. Severin, …, A. A. Hyman. 2007. Straight GDP-tubulin protofilaments form in the presence of taxol. *Curr. Biol.* 17:1765–1770.
48. Hess, H., J. Clemmens, …, V. Vogel. 2005. Molecular self-assembly of "nanowires"and "nanospools" using active transport. *Nano Lett.* 5:629–633.
49. Ziebert, F., H. Mohrbach, and I. M. Kulić. 2015. Why microtubules run in circles: mechanical hysteresis of the tubulin lattice. *Phys. Rev. Lett.* 114:148101.
50. Pearce, S. P., M. Heil, …, A. Prokop. 2018. Curvature-sensitive kinesin binding can explain microtubule ring formation and reveals chaotic dynamics in a mathematical model. *Bull. Math. Biol.* 80:3002–3022.
51. Mehrbod, M., and M. R. K. Mofrad. 2011. On the significance of microtubule flexural behavior in cytoskeletal mechanics. *PLoS One.* 6:e25627.
52. Tang, Z., N. A. Kotov, …, B. Ozturk. 2003. Nanostructured artificial nacre. *Nat. Mater.* 2:413–418.
53. Shao, Z., and F. Vollrath. 2002. Surprising strength of silkworm silk. *Nature.* 418:741.
54. Rho, J. Y., R. B. Ashman, and C. H. Turner. 1993. Young's modulus of trabecular and cortical bone material: ultrasonic and microtensile measurements. *J. Biomech.* 26:111–119.
55. Cox, H. L. 1952. The elasticity and strength of paper and other fibrous materials. *Br. J. Appl. Phys.* 3:72–79.
56. Buée, L., T. Bussière, …, P. R. Hof. 2000. Tau protein isoforms, phosphorylation and role in neurodegenerative disorders. *Brain Res. Brain Res. Rev.* 33:95–130.